Nanoscale

Accepted Manuscript

This article can be cited before page numbers have been issued, to do this please use: P. Jiang, C. Chang, C. Hsieh, W. Su and J. Tsay, *Nanoscale*, 2020, DOI: 10.1039/C9NR10053A.

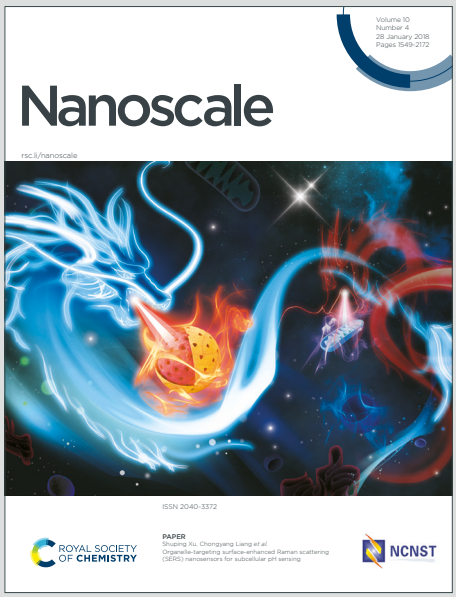

ROYAL SOCIETY OF CHEMISTRY

rsc.li/nanoscale

DOI: 10.1039/C9NR10053A

A practical method for fabricating superparamagnetic films and the mechanism involved

Pei-Cheng Jiang,[1,2,#] Cheng-Hsun-Tony Chang,[3,#] Chen-Yuan Hsieh,[1] Wei-Bin Su,[2] and Jyh-Shen Tsay[1,*]

[1]*Department of Physics, National Taiwan Normal University, Taipei 116, Taiwan*

[2]*Institute of Physics, Academia Sinica, Taipei 11529, Taiwan*

[3]*Department of Electronic Engineering, Minghsin University of Science and Technology, Hsinchu 30401, Taiwan*

Abstract

Due to the widespread applications of biosensors, such as in magnetic resonance imaging, cancer detection and drug delivery, the use of superparamagnetic materials for preparing biosensors has increased greatly. We report herein on a strategy toward fabrication of a nanoscale biosensor comprised of superparamagnetic films. By increasing the film thickness of magnetic layers, a phase transition typically occurs from either a low-Curie-temperature state or a superparamagnetic state to a ferromagnetic state. A new finding is demonstrated wherein a phase transition of such a superparamagnetic phase can be induced by controlling the thickness of ultrathin ferromagnetic layers with perpendicular magnetic anisotropy. Both the *M-H* curve with zero coercive force at 300 K and deviations for the normalized hysteresis loop at 2 K confirm the superparamagnetic state for Co/Ir(111) at room temperature. An overstrained film transforming to clusters (OFTC) model based on the new finding and our experimental evidence is proposed for modeling this phenomenon. From the energetic point of view of the OFTC model, we propose a limited distortion mechanism that can be useful in determining the critical thickness for the phase transition. This mechanism considers the balance between interfacial strain energy and surface free energy. A method for producing superparamagnetic films by taking advantage of the accumulation of strain and relaxation is reported.

Keywords: superparamagnetic film, cobalt, strain, biosensor, magneto-optical Kerr

View Article Online
DOI: 10.1039/C9NR10053A

effect.

---

*To whom correspondence should be addressed. Electronic mail: jstsay@phy.ntnu.edu.tw. Telephone: +886-2-77346031. Fax: +886-2-29326408.
#These authors contributed equally to this work.

†Electronic supplementary information (ESI) available.

View Article Online
DOI: 10.1039/C9NR10053A

In recent years, extensive explorations into biosensors composed of superparamagnetic materials have been carried out because of their widespread applications such as magnetic resonance image (MRI), cancer detection and target drug delivery [1-8]. For example, hydrophilic and surface-functionalized superparamagnetic iron oxide nanoparticles are promising heat-inducing agents for use in magnetic fluid hyperthermia-based thermotherapy and could be used as effective nanomedicines for cancer treatment [1]. By exploiting the superparamagnetic and plasmonic properties of core-shell nanomaterials, a label-free, high throughput cytokine immunoassay was realized on a large surface area with a remarkable degree of tunability and scalability [2]. Polymer coronas decorated with ultra-small superparamagnetic nanoparticles have shown significant contrast enhancement in *in vivo* MRI tests and efficient anticancer drug delivery characteristics, leading to the inhibition of tumor growth [6]. Biocompatible magnetite nanoparticles, prepared by post-coating magnetic nanocores with a synthetic polymer, could efficiently shield the particles from nonspecific interactions with cells [8].

To fabricate superparamagnetic materials, the magnetic anisotropy energy (MAE) of a system in achieving a superparamagnetic phase transition from a ferromagnetic phase, is a key issue. The MAE of a magnetic structure depends on the species, size, shape, crystalline form and strain of the ferromagnetic grains being used, and is related to the magnetic phase transition [9-15]. Ultrathin Co on Pt(111) exhibits a perpendicular magnetic anisotropy (PMA) at lower coverage and undergoes a spin reorientation transition (SRT) to an in-plane magnetic anisotropy at higher coverage owing to the strong spin-orbital coupling at the interface [14]. The magnetocrystalline effect overcomes the effect of roughness and strongly dominates the coercive force of Co/Si(100) films. By increasing the rubrene concentration, more Co/rubrene interfaces are introduced in composite films and the additional rubrene serves as a surfactant that

View Article Online
DOI: 10.1039/C9NR10053A

enhances the quality of the films [15]. For ferromagnetic particles below a critical size, the remanent magnetization is no longer fixed in the direction dictated by the MAE and the ambient thermal energy may cause a magnetic moment jump between two stable orientations of magnetization thus showing superparamagnetic behavior [11,12]. Below the superparamagnetic limit, a particle has no memory of its remanent state and shows no coercivity.

Improving the sensitivity of biosensor is of importance for cancer detection in the early stage and in inhibiting tumor growth. From the literature, there are two classical methods for fabricating superparamagnetic materials [9,10]. One is producing nanoparticles using a solution process [9] while the other involves producing dispersed nanoparticles by evaporation on a solid substrate under a vacuum [10]. In both procedures, each superparamagnetic nanoparticle shows an isolated magnetic domain with a randomly oriented magnetization due to thermal agitation. By increasing the particle size, a magnetic phase transition typically occurs from a superparamagnetic phase to a ferromagnetic phase, resulting in magnetic domain evolution [11,12]. The preparation of superparamagnetic thin films or larger superparamagnetic nanoparticles, however, remains a challenge. In this contribution, we report on a new finding that a phase transition of a superparamagnetic phase can be induced by controlling the thickness of ultrathin ferromagnetic layers with PMA. An overstrained film transforming to clusters (OFTC) model based on the new finding and our experimental evidence is proposed for modeling this phenomenon. From the energetic point of view of the OFTC model, we propose a limited distortion mechanism that can be useful in determining the critical thickness for the phase transition. By taking advantage of strain accumulation and relaxation in the specimens, a method for producing superparamagnetic films is reported.

The preparations of the specimens were carried out in an ultrahigh vacuum (UHV)

View Article Online
DOI: 10.1039/C9NR10053A

chamber with a base pressure below 2×10^{-10} Torr, as measured using an ion gauge, and residual gases were checked using a quadrupole mass spectrometer. The surface of an iridium crystal was oriented within 0.5◦ of the (111) plane, as evidenced by x-ray Laue back reflection. The surface of the specimen was cleaned by cycles of Ar^+ ion sputtering and annealing at 900 K until a well-ordered p(1×1) pattern of low-energy electron diffraction (LEED) with bright, sharp spots and a low background intensity was observed. The morphology of the Ir(111) surface was monitored using an in-house constructed scanning tunneling microscope (STM) operated at 80 K. The chemical purity of the surface was checked using Auger electron spectroscopy (AES). Auger electrons were collected using an OMICRON hemispherical analyzer with an angular resolution of 2^o at distance of 30 mm. High-purity cobalt (99.997%) was deposited on the surface at room temperature from an in-house fabricated, well-collimated evaporator [16]. The cobalt coverage was determined from the Auger signal ratio and confirmed by STM. The surface of the iridium single crystal was cleaned after each cobalt overlayering. A He-Ne laser with a wavelength of 632.8 nm was used as the light source for the magneto-optical Kerr effect (MOKE) measurements. The magnetic field was applied in-plane and perpendicular to the surface of the specimen in the longitudinal and the polar configurations, respectively. The various components have been described in detail elsewhere [17-22]. The magnetic moments of Co/Ir(111) film was measured by a commercial SQUID magnetometer (Quantum Design, San Diego) in a sealed capsule at 300 K, 200 K, 100 K, and 2 K [23,24]. By applying a cyclic external magnetic field between 10 kOe and -10 kOe, a clear magnetic hysteresis cycle was observed (see results and discussion for Figure 3).

Co overlayers were deposited on the top of the Ir(111) surface to investigate the corresponding magnetic properties. Figure 1a shows Kerr signals versus the magnetic field for Co/Ir(111) up to 8 monolayers (ML) in both the longitudinal and polar

configurations. Hysteresis occurs only in the polar configuration with increasing Co thickness. No hysteresis was detected in the longitudinal configuration and therefore Co/Ir(111) films show PMA. The effective magnetic anisotropy energy K_{eff} [13] can be expressed by

$$K_{\mathrm{eff}} = (K_{\mathrm{s}}^{\mathrm{UHV/Co}} + K_{\mathrm{s}}^{\mathrm{Co/Ir}})/d_{\mathrm{Co}} + K_{\mathrm{v}}^{\mathrm{Co}} \quad (1);$$

where $K_{\mathrm{s}}^{\mathrm{UHV/Co}}$ and $K_{\mathrm{s}}^{\mathrm{Co/Ir}}$ are the interfacial contributions from UHV/Co and Co/Ir, respectively; $K_{\mathrm{v}}^{\mathrm{Co}}$ is the volume contribution; d_{Co} is the Co thickness. From the literature, the interfacial magnetic anisotropies $K_{\mathrm{s}}^{\mathrm{UHV/Co}}$ and $K_{\mathrm{s}}^{\mathrm{Co/Ir}}$ are -0.17 mJ/m^2 and +0.80 mJ/m^2, respectively, while the volume contribution $K_{\mathrm{v}}^{\mathrm{Co}}$ is -0.74 MJ/m^3 [13,25,26]. Since interfacial contributions effectively exhibit a positive value ($K_{\mathrm{s}}^{\mathrm{UHV/Co}} + K_{\mathrm{s}}^{\mathrm{Co/Ir}}$=+0.63 mJ/m^2), the PMA is preferred for ultrathin Co overlayers on Ir(111). Considering the negative value of the volume contribution $K_{\mathrm{v}}^{\mathrm{Co}}$, the SRT from PMA to in-plane magnetic anisotropy should occur for thicker Co/Ir(111) films. However, by increasing the Co thickness, the hysteresis unexpectedly vanishes showing that ferromagnetism disappears in the case of 8 ML Co/Ir(111). Since only the polar Kerr intensity is detectable, Figure 1b shows Kerr intensity and coercive force (H_{C}) versus Co thickness in the polar configuration. As the Co thickness increases below 6 ML, an increase in the polar Kerr intensity is observed. For magnetic films thinner than the skin depth of visible light, a proportional relation between the Kerr intensity and the film thickness would be expected [27,28]. However, below 6 ML, the Kerr intensity increases with different slopes. For Co/Ir(111) layers thicker than 8 ML, the Kerr intensity drops to a zero value. Both the changed slope for Kerr intensity (< 6 ML) and the disappearance of ferromagnetism (> 8 ML) could be related to a structural change in Co/Ir(111), which is discussed below.

View Article Online
DOI: 10.1039/C9NR10053A

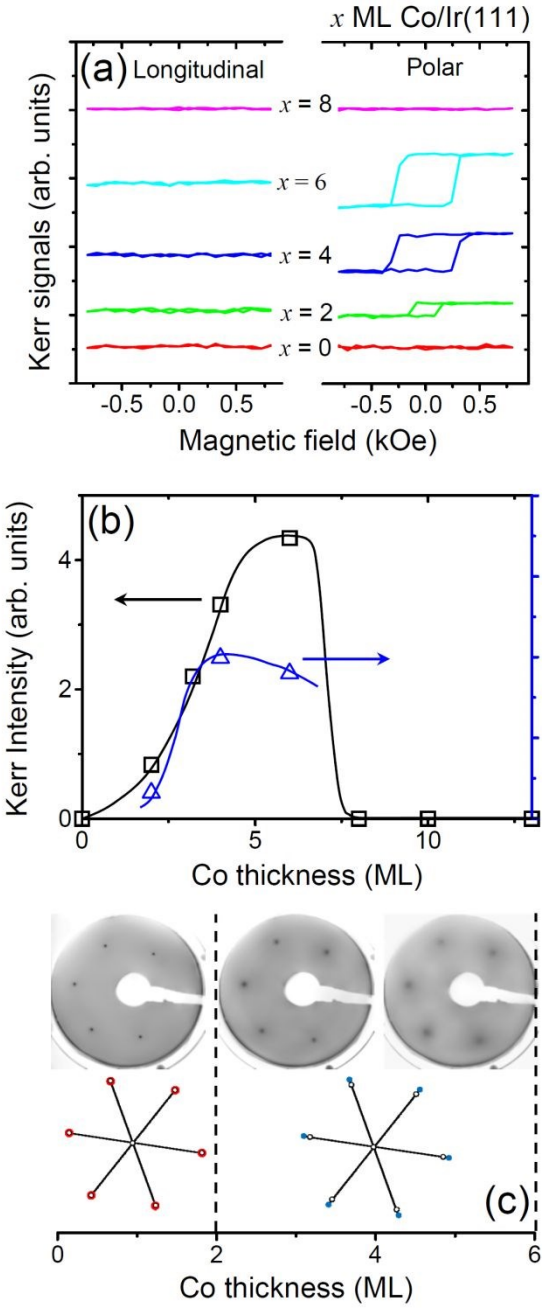

Figure 1. (a) Kerr signals versus magnetic field for Co/Ir(111) in both the longitudinal and polar configurations. The curves for x=0 corresponds to the Ir(111) substrate. (b) Kerr intensity and coercive force versus Co thickness in the polar configuration. (c) LEED patterns for 2, 4, and 6 ML. The lowered panel shows schematic LEED patterns for the strained and relaxed Co.

Because of the finite inelastic mean free path for low-energy electrons, LEED is

View Article Online
DOI: 10.1039/C9NR10053A

very surface sensitive [29,30]. For an Ir(111) surface, a hexagonal LEED pattern with a three-fold symmetry was observed. From the positions of the primary beams, the in-plane lattice parameter was a_{Ir}=2.72 Å and can be used in the further analyses [19,20]. For a Co/Ir(111) layer thinner than 3 ML, a p(1×1) LEED pattern was observed and this shows that the Co overlayer undergoes pseudomorphic growth. Co layers are strained due to the lattice mismatch at the Co/Ir interface. From Figure 1c, the in-plane lattice parameter for the Co layers is a_{Co}=2.72 Å, essentially the same as that of the Ir(111) surface. As the thickness increases (> 4 ML), the full widths at half maximum (FWHM) of the LEED spots become larger (Figure 1c) while the in-plane lattice parameter increases to a value close to that of Co(0001). The schematic plots in Figure 1c show that the topmost layer of the strained Co is relaxed to a structure close to that for bulk Co. This morphological evolution of Co/Ir(111) was further explored by applying an STM technique.

Figure 2a shows the STM image of Co/Ir(111) at the initial stage of Co deposition. Co atoms are attached to the steps of Ir(111) terraces. As the Co coverage increases to around 2 ML (Figure 2b), a large amount of two-dimensional, hexagonally-shaped Co islands forms on the surface due to the condensation of Co atoms. The atomic heights of the islands are revealed from the line scan across the step edge. For 3 ML Co/Ir(111) (Figure 2c), the sizes of the hexagonal Co islands continue to grow and some smaller triangular islands start to form on the top of hexagonal islands. The observation of the atomic steps indicates layer-by-layer growth for Co/Ir(111) layers thinner than 3 ML. For thicker Co/Ir(111), the growth of small islands on the top of incomplete monolayers was observed as shown in Figures 2d and 2e. From the line scan across the step edge, the islands retain the characteristics of atomic heights. However, the surface morphology suggests that the growth behavior deviates from the layer-by-layer mode. As the Co thickness increases further up to 8 ML (Figure 2f), the surface morphology

View Article Online
DOI: 10.1039/C9NR10053A

changes to a cluster type. From the inset of the STM image in Figure 2f, uniform nanometer-sized clusters are distributed on the surface. No atomic step was detected from the line scan across the clusters. The Co clusters exhibit an oval shape and are isolated from each other. Further exploration shows that the characteristics of the isolated Co clusters with an oval shape remain unchanged at least up to 13 ML. When the size of a magnetic cluster shrinks, as a result of an amount of ambient thermal energy sufficient to cause magnetic moment jumping between two different stable orientations of magnetization, a phase transition from ferromagnetic to superparamagnetic behavior occurs. From the literature, the upper limit V_{SPM} of the cluster size related to the superparamagnetic state can be calculated by

$$K_u \cdot V_{SPM} = k_B \cdot T \qquad (2);$$

where K_u is the anisotropy energy; k_B is the Boltzmann constant; T is the temperature [11]. K_u is 4.1×10^5 J/m^3 for cobalt and $k_B \cdot T$ is 4.14×10^{-21} J at room temperature. The calculated upper limit for V_{SPM} is around 10 nm^3. From the STM images in Figure 2f, Co forms clusters for Co/Ir(111) layers thicker than 8 ML. The average size of the Co clusters for 8 ML Co/Ir(111) is 1.17±0.14 nm^3, a value that is well below the upper limit V_{SPM} of the cluster size related to the superparamagnetic state. From an energetic point of view, 8 ML Co/Ir(111) in a cluster type is therefore superparamagnetic. For superparamagnetic clusters, the anisotropy (saturation) field is typically larger than a few tesla [10,31,32]. In our MOKE measurements, the applied field (800 Oe) was determined to be much smaller and therefore no hysteresis is detectable for 8 ML Co/Ir(111). By increasing the thickness of the ferromagnetic layer supported on an iridium substrate, the transition from a ferromagnetic phase with PMA to a superparamagnetic phase was observed for the first time. When atoms are deposited on a substrate, the nucleation of adatoms usually causes the formation of small islands/clusters, large islands/clusters and then the formation of films. In case of

View Article Online
DOI:10.1039/C9NR10053A

deposition of magnetic atoms such as Fe, Co, and Ni, the Curie temperature always increases as the film thickness increases [33,34]. This shows typically a transition of low-Curie-temperature state to ferromagnetic state by increasing the film thickness [33,34]. For Co deposited on an Au(111) surface, as the amount of Co increases, a transition from superparamagnetism to ferromagnetism was observed [35]. On some vicinal surfaces, the localized diffusion of atoms on the terrace may cause the formation of superparamagnetic clusters followed by the formation of ferromagnetic films [36,37]. This typically shows a phase transition from either a low-Curie-temperature state or a superparamagnetic state to a ferromagnetic state by increasing the film thickness of magnetic layers. It is a "new finding" for Co/Ir(111) that a phase transition of such a superparamagnetic phase occurs by increasing the thickness of ferromagnetic layers. Based on the new finding of a phase transition of a superparamagnetic phase, we propose a strategy for preparing a new design of biosensor that is comprised of superparamagnetic films.

View Article Online
DOI: 10.1039/C9NR10053A

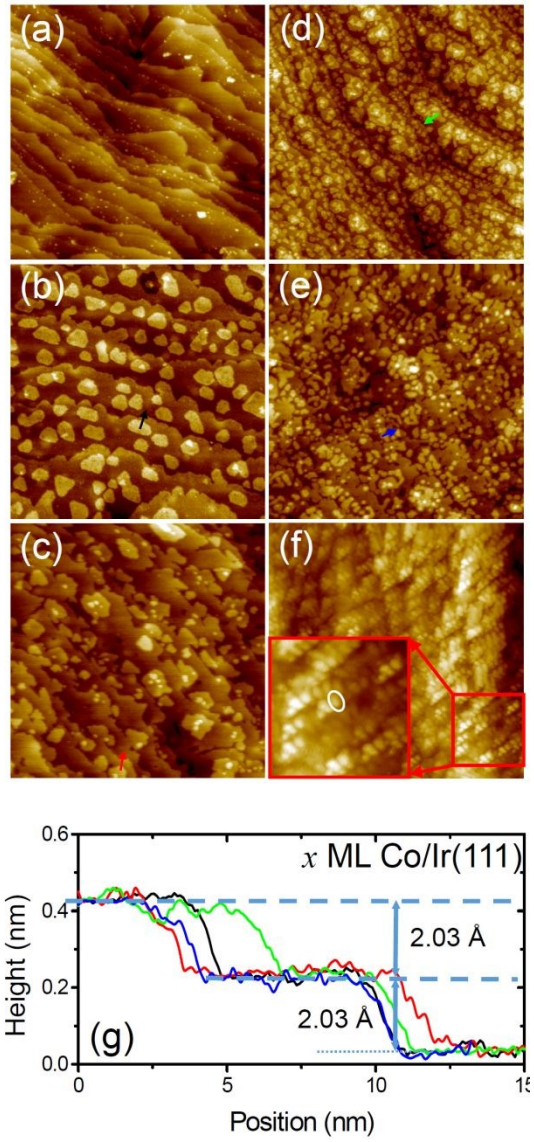

Figure 2. STM images for (a) 0.5 ML, (b) 2 ML, (c) 3 ML, (d) 4 ML, (e) 6 ML, and (f) 8 ML Co/Ir(111). The image size is 200×200 nm^2 for Figures 2a-2e and the image size is 100×100 nm^2 for Figure 2f. The inset of STM image in Figure 2f shows the oval-shaped Co clusters. (g) Line scans along the arrows in Figures 2b-2e showing the same step height of 2.03 Å.

In this study, the thickest Co/Ir(111) investigated is around 3 nm (13 ML). Since the skin depth of visible light in metal is in the order of a magnitude of 10 nm [38], the detection volume of MOKE covers the whole width range of Co/Ir(111). However, for superparamagnetic clusters, the anisotropy (saturation) field is typically larger than a

few tesla [10,31,32]. In our MOKE setup, the applied field (~800 Oe) is too small to assemble magnetization versus applied field (*M-H*) curve for 8 ML Co/Ir(111) at room temperature. We have performed the magnetization versus applied field (*M-H*) measurements using SQUID at low temperatures. Figure 3a shows the *M-H* curves for 8 ML Co/Ir(111) film at 300 K, 200 K, 100 K and 2 K with 10 kOe field. Superparamagnetic demagnetization occurs without coercivity because it is not the result of the action of an applied field but rather the thermal energy [11]. The field dependent magnetization curve with zero coercive force at room temperature is the most important feature for superparamagnetic materials [39-41]. As shown in Figure 3a, the *M-H* curve with zero coercive force at 300 K confirms that the sample is superparamagnetic. In additional, Figure 3b shows the normalized hysteresis loops (M/M_S *vs* H/T). In case of non-interacting superparamagnetic nanoparticles, normalized hysteresis loops should superpose above blocking temperature [42,43]. The normalized hysteresis loops (Figure 3b) obtained above 100 K in fact superpose while a deviation is observed for the normalized hysteresis loop at 2 K. By considering interactions of particle moments through long-ranged dipolar random forces, the interacting superparamagnetic (ISP) model explains very well where the hysteresis loops by ISP scaling should superpose [43-45]. Figure 3c shows the M/M_S *vs* H/M_S plot with ISP scaling and $m=M/M_S$ becomes a homogeneous function of the ratio H/M_S. Our SQUID measurements confirm the superparamagnetic state for 8 ML Co/Ir(111) film at room temperature.

View Article Online
DOI: 10.1039/C9NR10053A

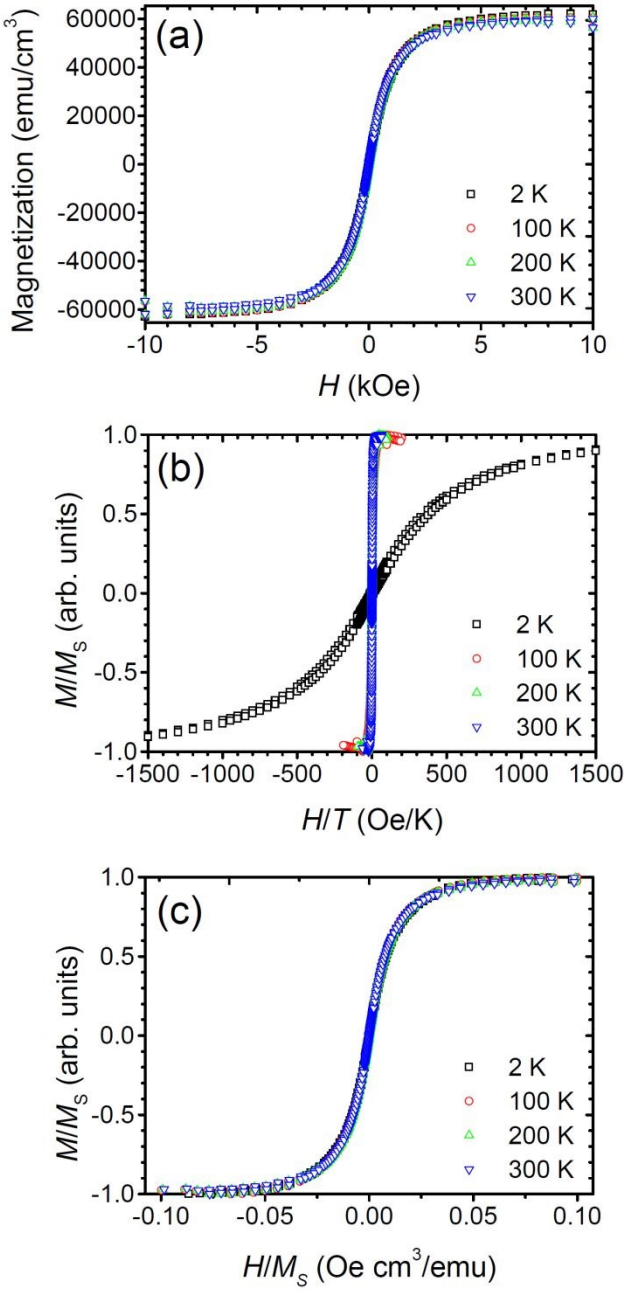

Figure 3 (a) Magnetization versus magnetic field (*M-H*) curves, (b) normalized hysteresis loops (M/M_S *vs H/T*), and (c) hysteresis loops by ISP scaling recorded at 300, 200, 100, 2 K for 8 ML Co/Ir(111).

Magnetic properties of Co/Ir(111) were investigated by employing SQUID magnetometry. As an example for 8 ML Co/Ir(111), ZFC and FC curves collected at *H* = 50 Oe are shown in Figure S1 (see the ESI† for details). The curves display the typical

View Article Online
DOI: 10.1039/C9NR10053A

behavior of superparamagnetic materials. The blocking temperature T_B, corresponding to the maximum in the ZFC curve, falls in the temperature range between 120 and 160 K. At temperature below T_B, the spins freeze and the system enter the blocked regime with typical out-of-equilibrium behavior [40,46-49]. The measured blocking temperature of 8 ML Co/Ir(111) is much higher than what we expected. This phenomenon has been previously observed for superparamagnetic nanoparticles in this size range (~1 nm^3) and are attributed to a significantly higher value of magnetocrystalline anisotropy [49-51]. From the literature, the median magnetic diameter of superparamagnetic nanoparticles can be calculated from the magnetic measurements [45,52-54]. As reported by Ferrari et al, the median magnetic moment of the particle can be calculated by refining the high temperature anhysteretic magnetization isotherms, using the Langevin function with a unimodal log-normal distribution [52,53]. For the real system of the superparamagnetic nanoparticles with a size distribution, the magnetization M of the nanoparticles in a magnetic field H can be written as a weighted sum of the Langevin functions [52,53]. From the volume distribution function $f(V_\mu)$ calculated from the M-H curve for 8 ML Co/Ir at 300 K, the median volume V_o and mean volume V_m of the superparamagnetic clusters are determined to be 1.236 and 1.242 nm^3, respectively (see the ESI† for details). As compared to the STM measurements (V_{STM}= 1.17±0.14 nm^3) as discussed in Figure 2, a well consistence of the determined volume is obtained.

From the literature, no alloy formation occurs after thermal annealing treatments for Co/Ir(111) below 773 K [55]. Figures 4a and 4b show STM images for 8 ML Co/Ir(111) before and after annealing at 550 K, respectively, which permitted the effects of a superparamagnetic phase to be explored after the thermal annealing treatments. The characteristics of isolated Co clusters were observed before the annealing treatment. Co clusters nucleate at a high temperature and are then

View Article Online
DOI: 10.1039/C9NR10053A

transformed into a continuous film with large terraces (Figure 4b). From the energetic point of view, the condition needed for the formation of the superparamagnetic phase is removed. Further MOKE measurements show that the hysteresis behavior is restored after a slight annealing at 400 K, as shown in Figure 4c. Both the saturation Kerr intensities and coercive forces increase after annealing at higher temperatures. This result unambiguously shows that the superparamagnetic phase is transformed to a ferromagnetic phase as the result of the nucleation of Co clusters to form Co films. We conclude that the unexpected disappearance of hysteresis behavior for 8 ML Co/Ir(111) in Figure 1 can be attributed to the formation of a superparamagnetic phase.

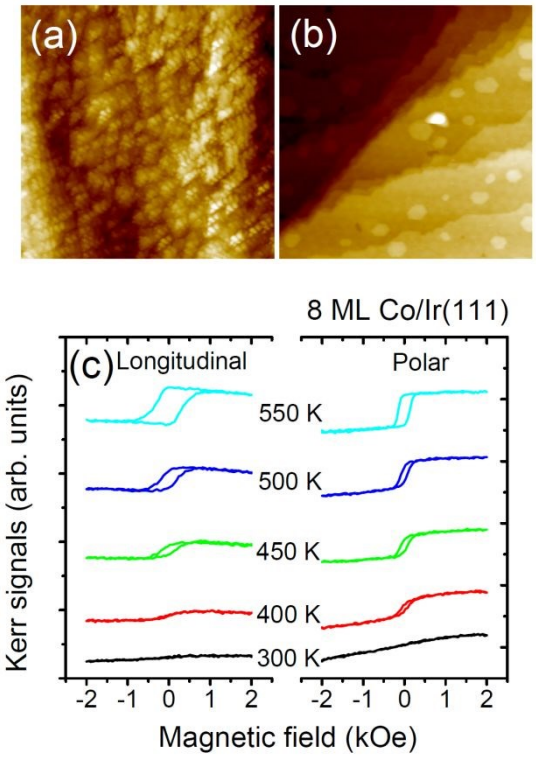

Figure 4. STM images of 8 ML Co/Ir(111) (a) before and (b) after annealing treatments. The image sizes are 100×100 nm^2. (a) Kerr signals versus magnetic field for 8 ML Co/Ir(111) at elevated temperatures in both the longitudinal and polar configurations.

Based on the magnetic measurements shown in Figures 1, 3 and 4c and the related

View Article Online
DOI: 10.1039/C9NR10053A

morphological evolution in Figures 2, 4a and 4b, we propose an OFTC model based on the experimental evidence showing that a thin-film form is changed into a cluster form. The OFTC model is schematically illustrated in Figure 5. For Co/Ir(111) thinner than 3 ML (Figure 5a), large two-dimensional islands form on the surface and the films are ferromagnetic with PMA. By increasing the Co thickness (Figure 5b), the growth behavior deviates from the layer-by-layer mode, while the ferromagnetic properties of the films persist. Further increasing the Co thickness above 8 ML (Figure 5c) results in the formation of nanometer-sized clusters because the Co films are no longer stable due to the great interfacial strain energy. As a result of the shrinking sizes of Co clusters, a phase transition from ferromagnetic to superparamagnetic behavior for Co/Ir(111) occurs and this is the core concept of the OFTC model. It is a new finding for Co/Ir(111) that a phase transition of such a superparamagnetic phase occurs by increasing the thickness of ferromagnetic layers. Based on the new finding of a phase transition of a superparamagnetic phase, we propose a strategy for preparing a new design of biosensor that is comprised of superparamagnetic films. Based on the OFTC model which describes a method for producing superparamagnetic films, we propose a superparamagnetic film on a microchip (SFoM) device in which the total magnetic moment can be further enhanced by 500 times as compared to commercial MRI contrast agents that use superparamagnetic nanoparticles (see the ESI† for details). After the thermal annealing treatments (Figures 5d), Co clusters nucleate and are transformed into a continuous film with large terraces and the superparamagnetic phase is restored to a ferromagnetic phase.

View Article Online
DOI: 10.1039/C9NR10053A

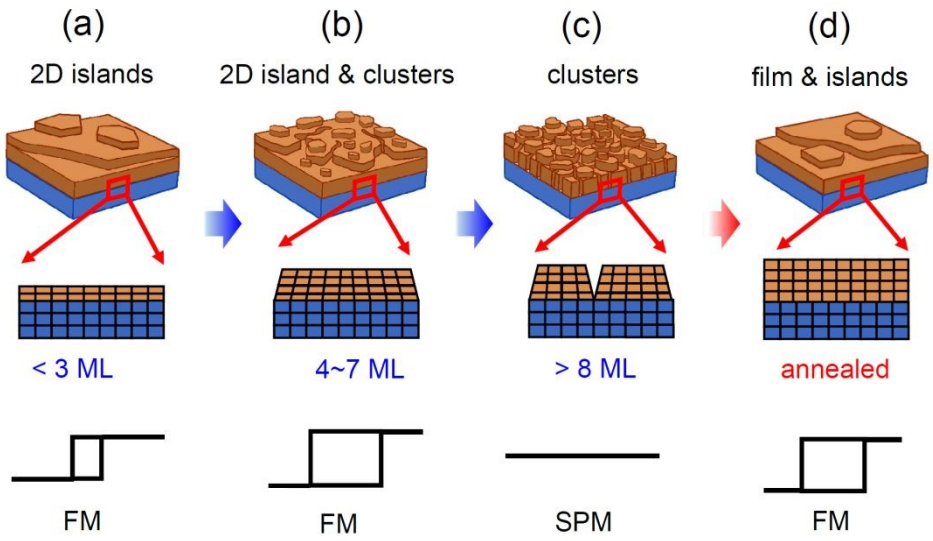

Figure 5. A schematic plot showing the OFTC model for describing the morphological evolution and related magnetic phase transition for Co/Ir(111) with thickness (a) < 3 ML, (b) 4~7 ML, (c) >8 ML, (d) after an annealing treatment.

In order to explain the driving force for the transformation of a ferromagnetic phase to a superparamagnetic phase, the OFTC model propose a limited distortion mechanism that takes the interfacial strain energy E_i and the surface free energy E_s into consideration. As atoms are deposited on a substrate to form a heterogeneous interface, we start with the atomic interactions, consisting mainly of the cohesive force between adatoms, and the interfacial adhesive force between adatoms and the substrate. Cohesive force is an attractive force between adatoms with an electrical attraction that can maintain a microscopic structure. From the energetic point of view, the cohesive force is related to the surface free energy. For a heterogeneous interface with a lattice mismatch, lattice distortion causes the storage of stain energy as a result of the competition between the adhesive force of adatoms and the interfacial adhesive force [56,57]. As the thickness of the adlayer increases, interfacial strain energy E_i increases accordingly. The increasing E_i may reach the value of the surface free energy E_s at a critical thickness. In order to release the lattice distortion, the strained layers are

View Article Online
DOI: 10.1039/C9NR10053A

transformed into loose clusters for Co/Ir(111) above the critical thickness.

Schematics of the original Co bulk unit cell (black) and the Co unit cell strained at the surface (red) are shown in Figure 6a; where *a* is the in-plane lattice parameter; *c* is out-of-plane lattice parameter equal to the layered distance; and *V* is the volume of unit cell. In the STM measurements, *c* is related to the height of the atomic steps. For a hexagonal structure, the strain energy density E_ρ can be expressed as

$$E_\rho = \frac{c_{11}}{2}(\varepsilon_1+\varepsilon_2)^2 + \frac{c_{33}}{2}\varepsilon_3^2 + \frac{c_{44}}{2}(\varepsilon_4^2+\varepsilon_5^2) + c_{66}\left(\frac{\varepsilon_6^2}{4}-\varepsilon_1\varepsilon_2\right) + c_{13}(\varepsilon_1+\varepsilon_2)\varepsilon_3 \quad (3);$$

where the ε_i, i=1-6, are the components of the strain tensor in the crystal axes (unit vectors in the [100], [010], [001] directions) [58,59]. The variations of *a*, *c* and *V* for a distorted lattice as compared to the original lattice are defined as δa, δc and δV. In Figure 6a, the δa and δc represent lattice parameter changes of $a'-a$ and $c'-c$, respectively. The distortion ratio of the Co lattice ($\delta V/V$) can be expressed in terms of strain components as

$$\frac{\delta V}{V} = 2\frac{\delta a}{a} + \frac{\delta c}{c},\ \frac{\delta(c/a)}{(c/a)} = \frac{\delta c}{c} - \frac{\delta a}{a} \qquad (4)\ [59,60].$$

In materials science, the bulk modulus *B* describes the compressibility of a substance and the shear modulus *G* describes the relation between shear stress and shear strain. From the literature [59], the bulk modulus *B* and shear modulus *G* can be expressed as $B=(c_{33}+2c_{13})/3$ and $G=(c_{33}-c_{13})/2$, respectively. Equation (3) can be written as

$$E_\rho = \frac{B}{2}\left(\frac{\delta V}{V}\right)^2 + \frac{2G}{3}\left[\frac{\delta(c/a)}{(c/a)}\right]^2 \qquad (5).$$

V and c/a are orthogonal coordinated for the description of hexagonal distortion. The strain energy density E_ρ associated with the distortion of the Co lattice can be derived as Equation (5). Considering the thickness of the strained layer, the interfacial strain energy E_i can be expressed as

$$E_i = E_\rho \cdot t_{Co} \qquad (6)$$

View Article Online
DOI: 10.1039/C9NR10053A

where t_{Co} is the layered distance of deposited Co layers. Based on the lattice constants of bulk Ir(111) and Co(0001), the distortion ratio of the Co lattice ($\delta V/V$) and interfacial strain energy E_i can be calculated. In Figure 6b, the layered distances and the in-plane lattice parameters can be evaluated from the structural data shown in Figures 1c and 2. For a Co/Ir(111) layer thinner than 3 ML, the in-plane lattice parameter of a Co layer is 2.72±0.01 Å which is the same as that of the Ir(111) lattice. In addition, the layered distance is 2.03±0.01 Å which is the same as half of the *c*-axis of hcp-Co for strained layers. For a Co/Ir(111) layer with a thickness between 4 and 6 ML, a reduced in-plane lattice parameter for a Co layer of 2.59±0.01 Å for loose clusters is observed while the layered distance remains nearly unchanged. Because of the strain, at thicknesses above 8 ML, the layers are completely transformed into loose clusters. The diffraction peak is broadened too much to permit the in-plane parameter and layered distance to be accurately estimated. By substituting the values for the in-plane lattice parameter *a*, the layered distance *c*, the bulk modulus *B* (=1.28), and the shear modulus *G* (=1.87) for Co/Ir(111) into Equations (4), (5) and (6), the interfacial strain energy E_i versus the Co thickness can be evaluated, as shown in Figure 6c (black line). For 4 ML Co/Ir(111) as an example, the interfacial strain energy is 2.84 J/m^2 by substituting the values *a*=2.72 (Å), *c*=2.03 (Å), $\frac{\delta V}{V}$=0.167, $\frac{\delta(c/a)}{(c/a)}$=-0.0837 into Equations (4), (5) and (6). By comparing the stain energy and surface free energy, a critical thickness occurs at 4 ML estimated for Co/Ir(111). The good agreement between the measured results and the calculated energy results suggests that the limited distortion mechanism is useful for correlating the increasing of the interfacial strain energy E_i and the surface free energy E_s.

View Article Online
DOI: 10.1039/C9NR10053A

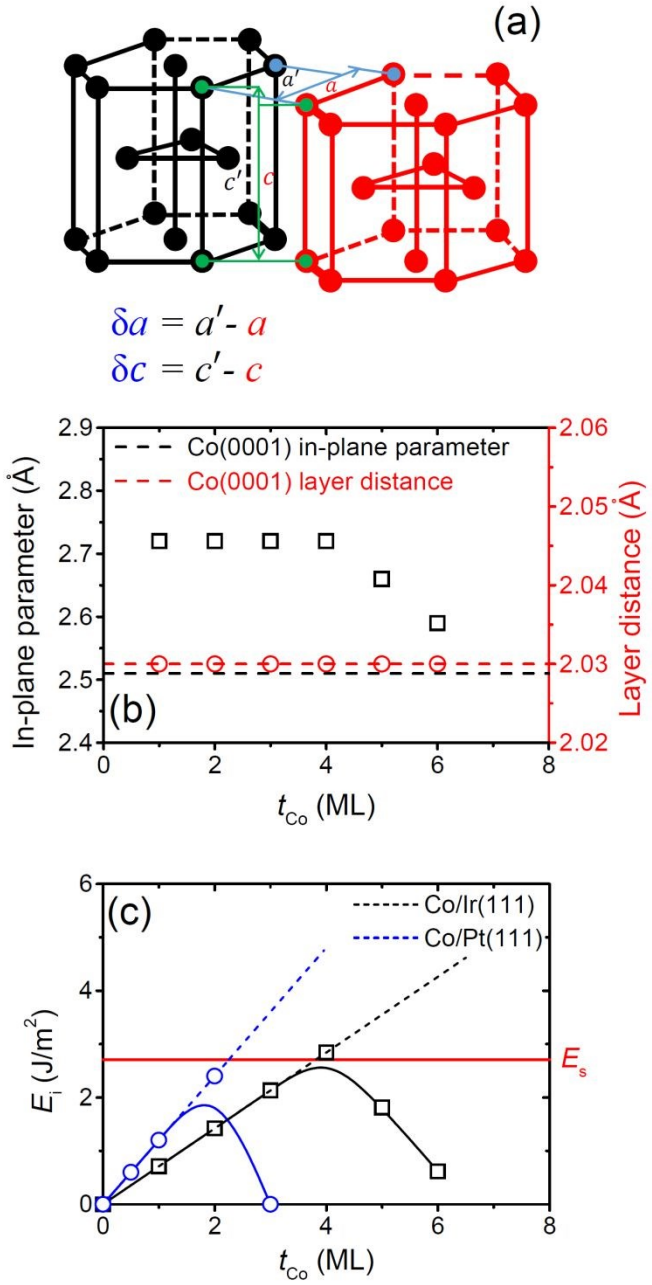

Figure 6. (a) Schematics showing the original Co bulk unit cell (black) and Co unit cell strained at the surface (red). (b) Layered distances (red) and the in-plane lattice parameters (black) versus Co thickness for Co/Ir(111). The black and red dashed lines show the in-plane lattice parameter and layered distance of Co(0001), respectively. (c) The interfacial strain energy E_i versus the Co thickness for Co/Ir(111) (black) and Co/Pt(111) (blue). The black and red dashed lines show the extrapolations of the linear parts of the interfacial strain energy E_i for Co/Ir(111) and Co/Pt(111) respectively. The

View Article Online
DOI: 10.1039/C9NR10053A

solid red line corresponds to the surface free energy of Co [61].

The limited distortion mechanism can be further applied to other systems. As an example of Co grown on a Pt(111) surface, the Co nucleates spatially in a homogeneous manner and quasi layer-by-layer growth occurs up to 3 ML followed by three-dimension island growth for thicker films [62]. From a detailed analysis of the STM images, the first-layer islands consist of locally coherent regions about 5 nm in diameter decorated by second-layer Co clusters, while these coherent regions are interrupted by localized defects [62]. The phenomenon of the formation of coherent regions followed by island growth for Co/Pt(111) is similar to the growth behavior of Co/Ir(111). Our previously reported LEED data for 2 ML Co/Pt(111) shows that the in-plane lattice parameter and layered distance are 2.78 Å and 2.03 Å, respectively [63]. Following the above discussions and substituting the values for the in-plane lattice parameter and layered distance into Equations (5) and (6), the interfacial strain energy E_i versus the thickness of the Co for Co/Pt(111) can be evaluated as shown in Figure 6c (blue line). By increasing the Co thickness, the calculated interfacial strain energy increases and then approaches the value for the surface free energy of Co(0001) at around 2 ML Co/Pt(111). A smaller critical thickness of 2 ML for Co/Pt(111) can be explained by a larger lattice misfit for Co/Pt(111) as compared to a Co/Ir(111) system.

In conclusion, for Co/Ir(111) layers thinner than 3 ML, the pseudomorphic growth of a Co overlayer shows that the Co layers are strained due to lattice mismatch at the Co/Ir interface. For thicker Co/Ir(111) layers, the growth of small islands on the top of the incomplete monolayers is observed while the in-plane lattice parameter increases to a value close to that of Co(0001). As the Co thickness increases further up to 8 ML, the surface morphology changes to a cluster type. By increasing the thickness of the ferromagnetic layer supported on an iridium substrate, magnetic measurements

demonstrate that a phase transition exists from a ferromagnetic phase with PMA to a superparamagnetic phase for the first time. SQUID measurements of both the *M-H* curve with zero coercive force at 300 K and deviations for the normalized hysteresis loop (M/M_S *vs* H/T) at 2 K confirm the superparamagnetic state for Co/Ir(111) at room temperature. From the volume distribution function $f(V_\mu)$ calculated from the *M-H* curve for 8 ML Co/Ir at 300 K, the median volume V_o and mean volume V_m of the superparamagnetic clusters are determined to be 1.236 and 1.242 nm^3, respectively, that are well consistent with the STM measurements (V_{STM}= 1.17±0.14 nm^3). After an annealing treatment for Co/Ir(111) in the superparamagnetic phase, the Co clusters nucleate to form a continuous film and therefore the superparamagnetic phase is transformed back to ferromagnetic phase. In order to explain the driving force for the transformation of a ferromagnetic phase to a superparamagnetic phase, the OFTC model proposes a limited distortion mechanism that takes the interfacial strain energy and the surface free energy into account. To release lattice distortion, the strained layers are transformed into loose clusters for Co/Ir(111) layers above the critical thickness.

Acknowledgments

The authors wish to acknowledge financial support from the Ministry of Science and Technology of Taiwan under Contract Nos. MOST 108-2112-M-003-014 and MOST 107-2112-M-003-010. We appreciate the assistance of Professor Dr Milton S. Feather for the English editing of the manuscript. This article was also subsidized by the National Taiwan Normal University (NTNU), Taiwan. We appreciate the fruitful discussions and supports from Professor Shang-Fan Lee for the characterizations of superparamagnetic properties.

View Article Online
DOI: 10.1039/C9NR10053A

Reference

1 G. Kandasamy, A. Sudame, T. Luthra, K. Saini and D. Maity, Functionalized Hydrophilic Superparamagnetic Iron Oxide Nanoparticles for Magnetic Fluid Hyperthermia Application in Liver Cancer Treatment, *ACS Omega*., 2018, **3**, 3991-4005.

2 Y. Cai, J. Zhu, J. He, W. Yang, C. Ma, F. Xiong, F. Li, W. Chen and P. Chen, Magnet Patterned Superparamagnetic Fe_3O_4/Au Core-Shell Nanoplasmonic Sensing Array for Label-Free High Throughput Cytokine Immunoassay, *Adv. Healthc. Mater*., 2019, **8**, 1801478.

3 A. Adamiano, M. Iafisco, M. Sandri, M. Basini, P. Arosio, T. Canu, G. Sitia, A. Esposito, V. Iannotti, G. Ausanio, E. Fragogeorgi, M. Rouchota, G. Loudos, A. Lascialfari and A. Tampieri, On the use of superparamagnetic hydroxyapatite nanoparticles as an agent for magnetic and nuclear in vivo imaging, *Acta Biomater.*, 2018, **73**, 458-469.

4 S.T. Meikle, Y. Piñeiro, M. Bañobre López, J. Rivas and M. Santin, Surface functionalization superparamagnetic nanoparticles conjugated with thermoresponsive poly(epsilon-lysine) dendrons tethered with carboxybetaine for the mild hyperthermia-controlled delivery of VEGF, *Acta Biomater*., 2016, **73**, 235-242.

5 Y. Ha, S. Ko, I. Kim, Y. Huang, K. Mohanty, C. Huh and J.A. Maynard, Recent Advances Incorporating Superparamagnetic Nanoparticles into Immunoassays, *ACS Appl. Nano Mater*., 2018, **1**, 512-521.

6 Q. Liu, L. Song, S. Chen, J. Gao, P. Zhao and J. Du, A superparamagnetic polymersome with extremely high T2 relaxivity for MRI and cancer-targeted drug delivery, *Biomaterials*, 2017, **114**, 23-33.

7 F. Ciccullo, N.M. Gallagher, O. Geladari, T. Chassé, A. Rajca and M.B. Casu, A

Derivative of the Blatter Radical as a Potential Metal-Free Magnet for Stable Thin Films and Interfaces, *ACS Appl. Mater. Interfaces*, 2016, **8**, 1805-1812.

8 E. Illés, M. Szekeres, I.Y. Tóth, A. Szabó, B. Iván, R. Turcu, L. Vékás, I. Zupkó, G. Jaics and E. Tombácz, Multifunctional PEG-carboxylate copolymer coated superparamagnetic iron oxide nanoparticles for biomedical application, *J. Magn. Magn. Mater.*, 2018, **451**, 710-720.

9 J.A. Becker, R. Schäfer, R. Festag, W. Ruland, J.H. Wendorff, J. Pebler, S.A. Quaiser, W. Helbig and M.T. Reetz, Electrochemical growth of superparamagnetic cobalt clusters, *J. Chem. Phys.*, 1995, **103**, 2520-2527.

10 S. Padovani, I. Chado, F. Scheurer and J.P. Bucher, Transition from zero-dimensional superparamagnetism to two-dimensional ferromagnetism of Co clusters on Au(111), *Phys. Rev. B*, 1999, **59**, 11887-11891.

11 R.C. O'Handley, *Modern Magnetic Materials: Principles and Applications*, Wiley, New York (2000).

12 D. Jiles, *Introduction to Magnetism and Magnetic Materials,* 3rd ed. CRC (2016).

13 M.T. Johnson, P.J.H. Bloemen, F.J.A. den Broeder and J.J. de Vries. Magnetic anisotropy in metallic multilayers, *Rep. Prog. Phys*., 1996, **59**, 1409-1458.

14 M.T. Lin, C.C. Kuo, H.Y. Her, Y.E. Wu, J.S. Tsay and C.S. Shern, Magneto-optical response and increase in perpendicular magnetic anisotropy, *J. Vac. Sci. Technol. A*, 1999, **17**, 3045-3050.

15 Y.J. Hou, C.H.T. Chang, C.K. Yang, C.Y. Hsu, Y.W. Jhou and J.S. Tsay, Structural determination and magnetic properties for Co-rubrene composite films on Si(100), *Appl. Surf. Sci.*, 2015, **354**, 139-143.

16 C.H.T. Chang, S.C. Chang, J.S. Tsay and Y.D. Yao, Enhanced exchange bias fields for CoO/Co bilayers: influence of antiferromagnetic grains and mechanisms, *Appl. Surf. Sci.*, 2017, **405**, 316-320.

17 W.B. Su, C.L. Lin, W.Y. Chan, S.M. Lu and C.S. Chang, Field enhancement factors and self-focus functions manifesting in field emission resonances in scanning tunneling microscopy, *Nanotechnology*, 2016, **27**, 175705.

18 W.Y. Chan, D.C. Tsai, W.H. Chen, C.H.T. Chang and J.S. Tsay, Enhancement of the polar coercive force for annealed Co/Ir(111) ultrathin films, *J. Korean Phys. Soc.*, 2013, **62**, 1945-1949.

19 W.H. Chen, S.C. Wang, Y.W. Tseng, D.C. Tsai and J.S. Tsay, The formation of a surface alloy for Ag/Ir(111) ultrathin films, *Surf. Sci.*, 2011, **605**, 2045-2049.

20 J.S. Tsay and Y.S. Chen, Oxygen adsorption on ultrathin Co/Ir(111) films: Compositional anomaly, *Surf. Sci.*, 2006, **600**, 3555-3559.

21 J.S. Tsay and C.S. Shern, Diffusion and alloy formation of Co ultrathin films on Pt(111), *J. Appl. Phys.*, 1998, **80**, 3777-3781.

22 Y.T. Chow, B.H. Jiang, C.H.T. Chang and J.S. Tsay, Enhancing magnetic anisotropy energy by tuning the contact area of Ag and Ni at the Ag/Ni interface, *Phys. Chem. Chem. Phys.*, 2018, **20**, 1504-1512.

23 D. T. Ha, M. Yen, H. L. Yu, C. Kuo, C. Chen, A. Tanaka, L. Tsai, Y. Zhao, C. Duan, S. Lee, C. Chang, J. Juang and Y. Chu, Mechanically tunable exchange coupling of Co/CoO bilayers on flexible muscovite substrate, *Nanoscale*, 2020, DOI: 10.1039/C9NR08810E.

24 F. B. Abdulahad, D.-S. Hung and S.-F. Lee, Temperature dependence of static and dynamic magnetic properties in NiFe/IrMn bilayer system, *J. Mater. Res.*, 2014, **29**, 1237-1247.

25 P. Beauvillain, A. Bounouh, C. Chappert, R. Mégy, S. Ould-Mahfoud, J.P. Renard, P. Veillet, D. Weller and J. Corno, Effect of submonolayer coverage on magnetic anisotropy of ultrathin cobalt films M/Co/Au(111) with M=Au, Cu, Pd, *J. Appl. Phys.*, 1994, **76**, 6078-6080.

26 F.J.A. den Broeder, W. Hoving and P.J.H. Bloemen, Magnetic anisotropy of multilayers, *J. Magn. Magn. Mater.*, 1991, **93**, 562-570.

27 Z.Q. Qiu and S.D. Bader, Surface magneto-optic Kerr effect, *Rev. Sci. Instrum.*, 2000, **71**, 1243-1255.

28 C.H.T. Chang, W.H. Kuo, Y.C. Chang, J.S. Tsay and S.L. Yau, Tuning coercive force by adjusting electric potential in solution processed Co/Pt(111) and the mechanism involved, *Sci Rep.*, 2017, **7**, 43700.

29 G. Ertl and J. Küppers. *Low Energy Electrons and Surface Chemistry*. 2nd ed. Weinheim, VCH (1985).

30 J.S. Tsay, T. Mangen, R.-J. Linden and K. Wandelt, Comparative study of annealing effects for Cu/Pt(111) films with and without oxygen, *Surf. Sci.*, 2001, **866**, 482-485.

31 J.P. Chen, C.M. Sorensen and K. J. Klabunde, Enhanced magnetization of nanoscale colloidal cobalt particles, *Phys. Rev. B*, 1995, **51**, 11527-11532.

32 M.E. McHenry, S.A. Majetich, J.O. Artman, M. DeGraef and S.W. Staley, Superparamagnetism in carbon-coated Co particles produced by the Kratschmer carbon arc process, *Phys. Rev. B*, 1994, **49**, 11358-11363.

33 F. Huang, M. T. Kief, G. J. Mankey, and R. F. Willis, Magnetism in the few-monolayers limit: A surface magneto-optic Kerr-effect study of the magnetic behavior of ultrathin films of Co, Ni, and Co-Ni alloys on Cu(100) and Cu(111), *Phys. Rev. B* 1994, 49, 3962-3971.

34 J.S. Tsay, Y.D. Yao, C.S. Yang, W.C. Cheng, T.K. Tseng, and K.C. Wang, Surface magneto-optic Kerr effect study in ultrathin Co/Ge(111) and Co/Ge(100) films, *Surf. Sci.* 2002, 513, 93-97.

35 S. Padovani, I. Chado, F. Scheurer, and J. P. Bucher, Transition from zero-dimensional superparamagnetism to two-dimensional ferromagnetism of Co

View Article Online
DOI: 10.1039/C9NR10053A

clusters on Au(111), *Phys. Rev. B* 1999, 59, 11887-11891.

36 S. J. Steinmuller, M. Tselepi, G. Wastlbauer, V. Strom, D. M. Gillingham, A. Ionescu, and J. A. C. Bland, Spin dynamics in an ultrathin Fe film in the vicinity of the superparamagnetic/ferromagnetic phase transition, *Phys. Rev. B* 2004, 70, 024420.

37 Yu Shiratsuchi, Yasushi Endo, Masahiko Yamamoto, Transition from superparamagnetic to ferromagnetic state of ultrathin Fe films grown on inclined Al2O3(0001) substrates, *Thin Solid Films*, 2004, 464-465, 141- 145.

38 J. D. Jackson, *Classical Electrodynamics*, 3rd edn, John Wiley and Sons, New York, 1999.

39 L. Wang, Y. Zhang, T. Liu, Z. Zhang, H. Hu, J. Zou, Q. Jia and Z. Jiang, Ge_xSi_{1-x} Virtual-Layer Enhanced Ferromagnetism in Self-assembled $Mn_{0.06}Ge_{0.94}$ Quantum Dots Grown on Si Wafers by Molecular Beam Epitaxy, *Nanoscale*, 2020, **12**, 3997-4004.

40 H. Amiri, M. Mahmoudi and A. Lascialfari, Superparamagnetic colloidal nanocrystal clusters coated with polyethylene glycol fumarate: a possible novel theranostic agent, *Nanoscale*, 2011, **3**, 1022-1030.

41 D. Maggioni, P. Arosio, F. Orsini, A.M. Ferretti, T. Orlando, A. Manfredi, E. Ranucci, P. Ferruti, G. D'Alfonso and A. Lascialfari, Superparamagnetic iron oxide nanoparticles stabilized by a poly(amidoamine)-rhenium complex as potential theranostic probe, *Dalton Trans*, 2014, **43**, 1172-1183.

42 K.L. Lopez-Maldonado, P. de la Presa, I. Betancourt, J.R. Farias Mancilla, J.A. Matutes Aquino, A. Hernando and J.T. Elizalde Galindo, Superparamagnetic response of zinc ferrite incrusted nanoparticles, *J. Alloys Compd*, 2015, **637**, 443-448.

43 P. Allia, P. Tiberto, Dynamic effects of dipolar interactions on the magnetic behavior

of magnetite nanoparticles, *J Nanopart Res*, 2011 **13**, 7277–7293.

44 G. Barrera, P. Tiberto, P. Allia, B. Bonelli, S. Esposito, A. Marocco, M. Pansini and Y. Leterrier, Magnetic Properties of Nanocomposites, *Appl. Sci*, 2019, **9**, 212.

45 Paolo Allia, Marco Coisson, Paola Tiberto, Franco Vinai, Marcelo Knobel, M. A. Novak, and W. C. Nunes, Granular Cu-Co alloys as interacting superparamagnets, *Phys. Rev. B* 2001, **64**, 144420.

46 U. Jeong, X. Teng, Y. Wang, H. Yang and Y. Xia, Superparamagnetic Colloids: Controlled Synthesis and Niche Applications, *Adv. Mater.* 2007, **19**, 33.

47 R. H. Kodama, Magnetic nanoparticles, *J. Magn. Magn. Mater*. 1999, **200**, 359.

48 J. L. Dormann, D. Fiorani and E. Tronc, *Magnetic Relaxation in Fine Particle Systems, in Advances in Chemical Physics*, vol. XCVIII, ed. I. Prigogine and S. A. Rice, J. Wiley and Sons, 1997.

49 John Watt, Grant C. Bleier, Mariah J. Austin, Sergei A. Ivanov and Dale L. Huber, Non-volatile iron carbonyls as versatile precursors for the synthesis of iron-containing nanoparticles, *Nanoscale*, 2017, 9, 6632-6637.

50 A. H. Lu, E. L. Salabas and F. Schüth, Magnetic Nanoparticles: Synthesis, Protection, Functionalization, and Application, *Angew. Chem., Int. Ed*., 2007, **46**, 1222–1244.

51 T. C. Monson, E. L. Venturini, V. Petkov, Y. Ren, J. M. Lavin and D. L. Huber, Large enhancements of magnetic anisotropy in oxide-free iron nanoparticles , *J. Magn. Magn. Mater.*, 2013, **331**, 156–161.

52 E. F. Ferrari, F. C. S. da Silva, M. Knobel, Influence of the distribution of magnetic moments on the magnetization and magnetoresistance in granular alloys, *Phys. Rev. B* 1997, **56**, 6086-6093.

53 B. Pacakova, S. Kubickova, G. Salas, A. Mantlikova, M. Marciello, M.P. Morales, D. Niznansky, J. Vejpravova, The internal structure of magnetic nanoparticles determines the magnetic response, *Nanoscale*, 2017, **9**, 5129-5140.

54 M. El-Hilo, Nano-particle magnetism with a dispersion of particle sizes, *J. Appl. Phys.* 2012, **112**, 103915.

55 I. Carlomagno, J. Drnec, A. M. Scaparro, S. Cicia, S. Vlaic, R. Felici and C. Meneghini, Co-Ir interface alloying induced by thermal annealing, *J. Appl. Phys.*, 2016, **120**, 195302.

56 A. Pimpinelli and J. Villain, *Physics of Crystal Growth.* Cambridge, Cambridge University Press (1998).

57 I.V. Markov, *Crystal Growth for Beginners: Fundamentals of Nucleation, Crystal Growth, and Epitaxy*. Singapore, World Scientific (1995).

58 L.D. Landau and E.M. Lisfschitz, *Lehrbuch der Theoretischen Physik.* Berlin, Akademie-Verlag (1983).

59 M. Sambi and G. Granozzi, Strain analysis of epitaxial ultrathin films on Pt(111), *Sur. Sci.*, 1998, **400**, 239-246.

60 T. Kraft and P.M. Marcus, Elastic constants of Cu and the instability of its bcc structure, *Phys. Rev. B*, 1993, **48**, 5886-5890.

61 L. Vitos, A.V. Ruban, H.L Skriver and J. Kollár, The surface energy of metals, *Sur. Sci.*, 1998, **411**, 186-202.

62 P. Griitter and U.T. Durig, Growth of vapor-deposited cobalt films on Pt(111) studied by scanning tunneling microscopy, *Phys. Rev. B*, 1994, **49**, 2021-2029.

63 J.S. Tsay and C.S. Shern, Rotated incommensurate domains of Co ultrathin films on Pt (111), *Sur. Sci*., 1998, **396**, 319-326.

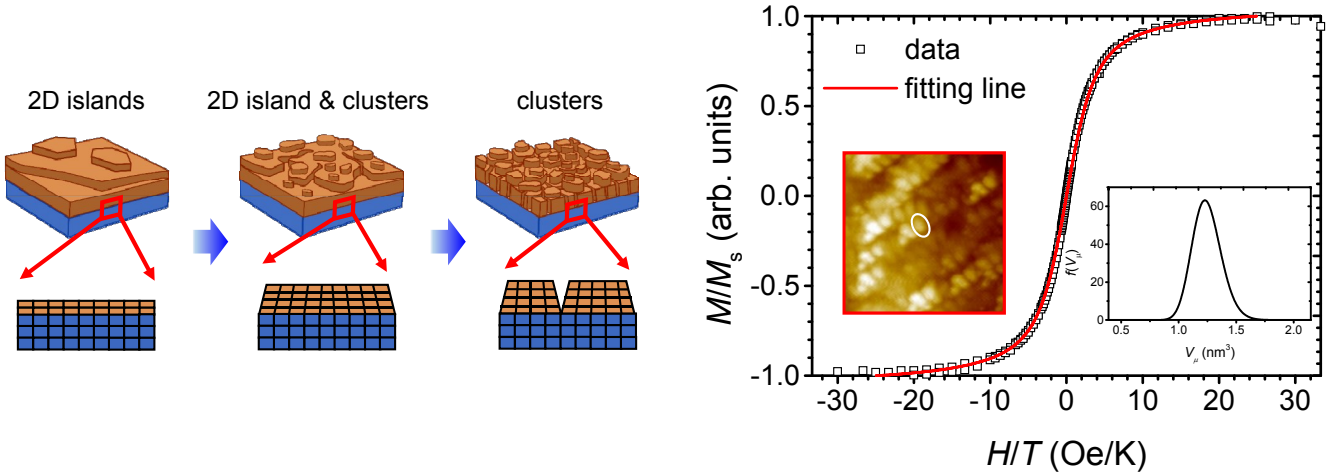

A schematic plot showing the OFTC model for describing the morphological evolution and magnetic phase transition to form a superparamagnetic state.